Supplementary Material

S.1 Photovoltaic Parameters of the Investigated Cells

Cell type	J_{SC} [mA/cm²]	V_{OC} [mV]	FF [%]	η [%]
no PDT, 50 nm	29.4	732	72.5	15.6
no PDT, 30 nm	29.2	654	61.1	11.7
no PDT, 20 nm	30.0	629	63.5	12.0
PDT, 50 nm	29.0	710	71.4	14.7
PDT, 30 nm	29.6	715	71.5	15.1
PDT, 20 nm	30.0	715	70.6	15.1

Table S.1: Current-voltage parameters of the investigated cell types: Short-circuit current density J_{SC}, open-circuit voltage V_{OC}, fill factor FF, and efficiency η. Mean values across 8–9 samples are given.

S.2 Breakdown Voltage

Several suggestions have been made in the literature on how to quantify the reverse voltage at which the blocking behaviour of the diode breaks down:

- Puttnins et al. [15] defined the breakdown voltage V_{br} via the intersection point of two straight lines fitted to the semilogarithmic $J(V)$ characteristics in voltage ranges before and after the breakdown.
- Szaniawski et al. [7] used a very similar approach, but on a semilog representation of the derivative $dJ(V)/dV$, to extract the "transition voltage" V_{tr}.
- Mansfield [16] on the other hand worked with a metric based on the dissipated power at the point where the reverse IV curve reaches the J_{MPP} of the device under STC. For our comparison below we used the voltage V_{jmp} at that point instead. That is, V_{jmp} is the voltage at which the current of the reverse IV curve under 70% illumination reached the J_{MPP} of the same sample under 100% illumination.

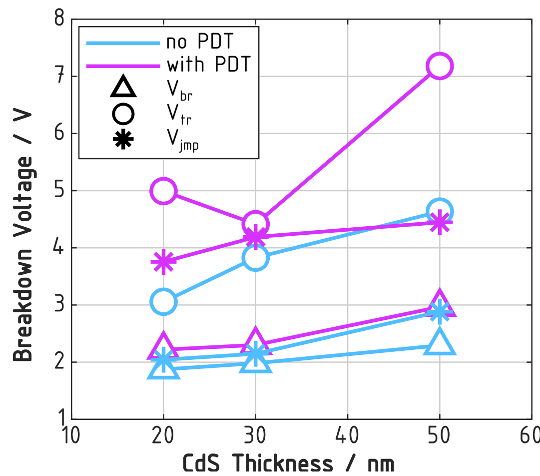

Figure S.1: Reverse breakdown voltages (absolute values) under white illumination for the cell types used in this study according to different definitions: V_{br} [15], V_{tr} [7], and V_{jmp} [16] (see text for details).

Fig. S.1 displays the breakdown voltages extracted from the averaged IV curves from Fig. 1a for the three definitions outlined above. Note that the uncertainty of the V_{tr} values

(circles in Fig. S.1) is relatively large because they are derived from differential data which is quite noisy for fast illuminated IV measurements. Keeping this in mind, all measures of breakdown voltage show the same qualitative trends (apart from one exception): The breakdown voltage increases with increasing CdS thickness, and it is larger for cells with PDT than for cells without PDT.

S.3 Tunneling Mechanism

In order to analyse the nature of the tunneling currents upon reverse breakdown in our samples, we checked whether the IV characteristics at breakdown are in line with the analytical expressions for the tunneling currents according to the Fowler-Nordheim and the Poole-Frenkel model [c.f. 7]. If the Fowler-Nordheim model applies in a certain voltage range, a plot of $(J - J_{\mathrm{SC}})/E^2$-vs-$1/E$ should be linear in that range. The data are shown in Fig. S.2a. Here, the electric field was calculated as $E = V_{\mathrm{applied}}/d_{\mathrm{CdS}}$. It seems that the data are indeed linear in a range of approximately 1 V above the breakdown voltages (bars and dashed lines, respectively). If the Poole-Frenkel model applies, a plot of $(J - J_{\mathrm{SC}})$-vs-$\sqrt{E}$ should be linear. The data are shown in Fig. S.2b. Similarly, the data show a linear dependence in a range of roughly 0.5–1 V above the breakdown voltages.

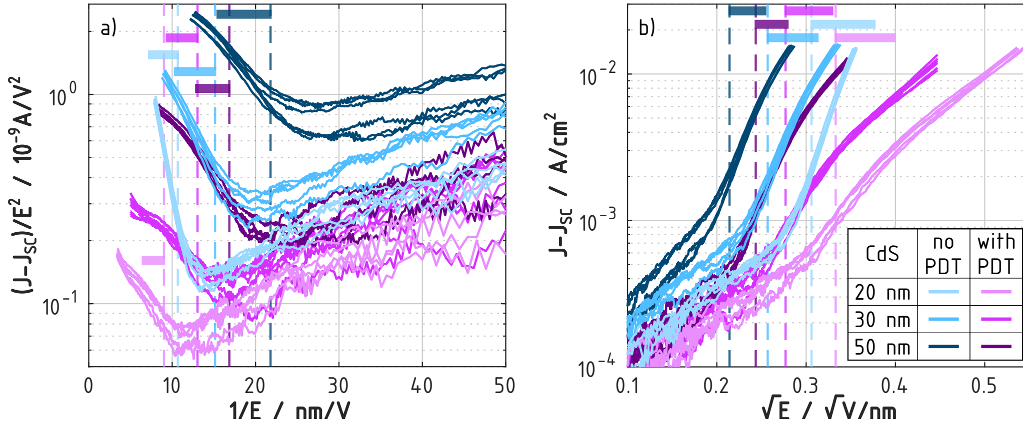

Figure S.2: Analysis of the reverse IV characteristics from Fig. 1a regarding a) the Fowler-Nordheim, and b) the Poole-Frenkel tunneling mechanisms. As a reference, dashed lines give the average breakdown voltages V_{br} according to the definition by Puttnins et al. [15] (cf. Sect. S.2) and attached bars indicate a range of −1 V.

S.4 Shunt Resistance under red and white illumination

Shunt resistances were extracted as the inverse slope of the IV curves of Fig. 1 in a range from −0.5 V to 0 V. It should be noted that, since the IV characteristics were recorded under illumination and very quickly (to prevent sample heating as much as possible), the data exhibit much more noise than the data from the dark-IV measurements in Fig. 4.

As for the shunt resistances extracted from dark IV measurements (Fig. 4), the average shunt resistances under illumination are larger for samples with PDT than for samples without PDT and increase with increasing CdS thickness for samples with PDT (although here the fluctuations in the data under white illumination do not allow for any reliable conclusions).

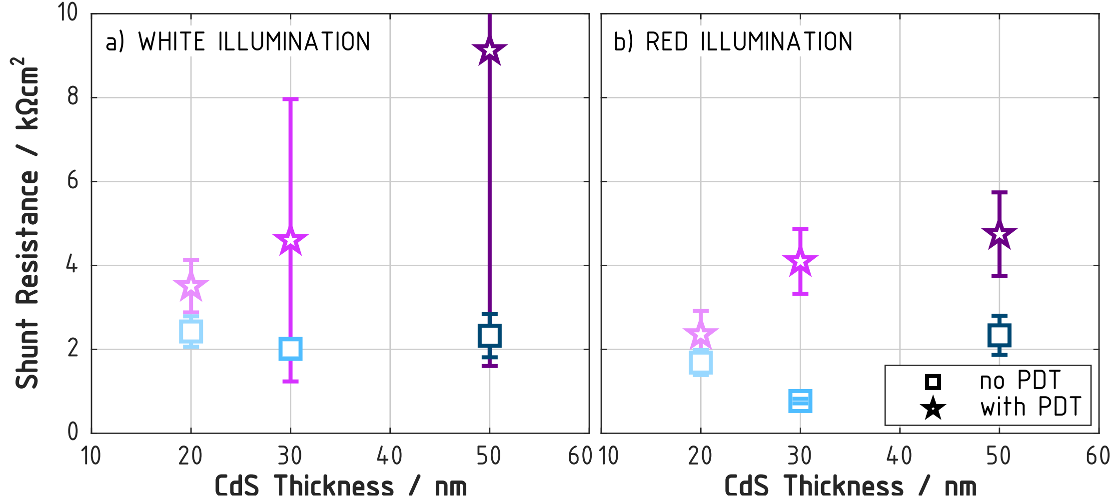

Figure S.3: Shunt resistances for all cell types in the case of a) white and b) red illumination. Mean values (symbols) and standard deviations (error bars) across the samples used in Fig. 1 are given.

For samples without PDT a clear trend with CdS thickness is not observed which may be due to interface recombination in samples with 20 nm and 30 nm CdS thickness (see main text).

S.5 Barrier Analysis of IVT

In order to further analyse the injection barrier observed in the temperature-dependent IV data in Fig. 3, we extracted the slope of the IV curve at V_{OC} and plotted it as a function of temperature in Fig. S.4 (symbols). Apparently the temperature at which the slope starts to drop when cooling down from room temperature is higher for the sample with PDT than for the sample without PDT, which indicates that the injection barrier is higher in the sample with PDT.

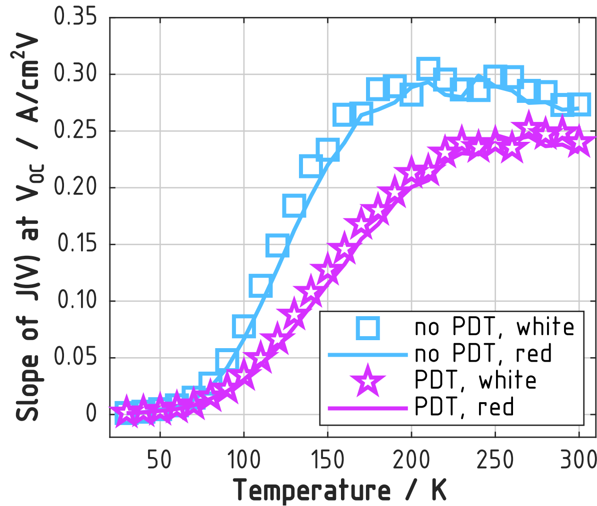

Figure S.4: Barrier analysis: Temperature-dependent slope of the IV curves from Fig. 3 at V_{OC} under white (symbols) and red (lines) illumination for a sample without PDT (blue) and with PDT (pink).

The same analysis was performed for measurements under red illumination ($\lambda > 610$ nm). The results are shown as solid lines in Fig. S.4. Obviously, there are no substantial differences in the barrier heights between the measurements under white and red illumination. In other words, the barrier is not sensitive to photoconductivity of the CdS buffer layer. This indicates that the responsible barrier may be located at the back interface. It is an interesting side note that this barrier is obviously affected by a RbF-PDT. Possibly, this is due to an accumulation of Rb at the interface between the absorber and the $MoSe_2$ layer [48].

S.6 Shunt Contribution of the P1 Scribe

Shunt resistances were extracted as the inverse slope of the dark IV characteristics in a range from −0.3 V to 0 V and are shown in Fig. S.5. Cells with three different widths of the P1 scribe (60, 90, and 200 µm) were fabricated and investigated. The analysis includes samples with PDT and a buffer thickness of 30 nm as well as samples without PDT and a buffer thickness of 50 nm.

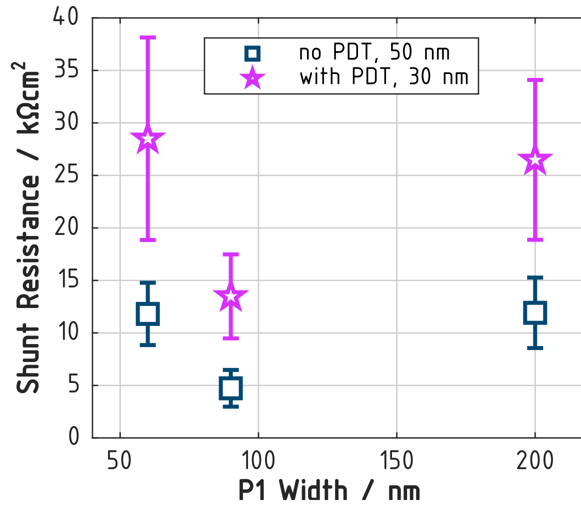

Figure S.5: Shunt resistance for cells with different widths of the P1 scribe. Mean values (symbols) and standard deviations (error bars) across 8–9 samples per cell type are given for cells without PDT and a buffer thickness of 50 nm and cells with PDT and a buffer thickness of 30 nm.

From the data in Fig. S.5 it is apparent that the relation between the shunt resistance and the P1 width is not strictly linear as we would expect if the shunt resistance was governed by the shunt path across the P1 scribe (the wider P1, the higher R_{sh}). Hence we assume that leakage currents across the P1 scribe do not represent a major shunt path in the investigated devices.